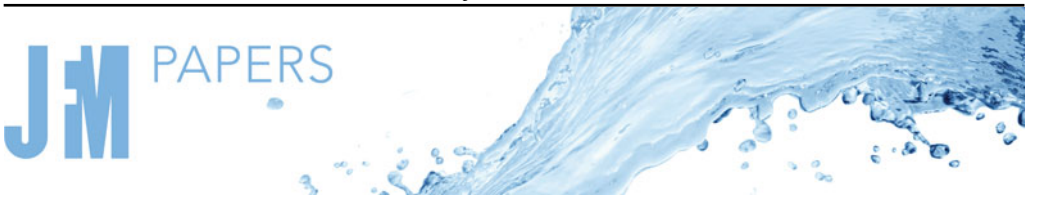
J. Fluid Mech. (2026), *vol.* 1037, A67, doi:10.1017/jfm.2026.11728



Extreme vortex gust encounters by a square wing

Hiroto Odaka[1], **Luke Smith**[1] **and Kunihiko Taira**[1]

[1]Department of Mechanical and Aerospace Engineering, University of California, Los Angeles, CA 90095, USA

Corresponding author: Hiroto Odaka, hodaka@g.ucla.edu

(Received 18 May 2025 UTC; revised 2 February 2026 UTC; accepted 22 May 2026 UTC)

Extreme gust encounters by finite wings with disturbance velocity exceeding their cruise speed remain largely unexplored, while being particularly relevant to miniature-scale aircraft. This study considers extreme aerodynamic flows around a square wing and the large, unsteady forces that result from gust encounters. We analyse the evolution of three-dimensional, large-scale vortical structures and their complex interactions with the wing by performing direct numerical simulations at a chord-based Reynolds number of 600. We find that a strong incoming positive gust vortex induces a prominent leading-edge vortex (LEV) on the upper surface of the wing, accompanied by tip vortices (TiVs) strengthened through the interaction. Conversely, a strong negative gust vortex induces an LEV on the lower surface of the wing and causes a reversal in TiV orientation. In both extreme vortex gust encounters, the wing experiences significant lift fluctuations. Furthermore, we identify two opposing effects of the TiVs on the large lift fluctuations. First, the enhanced or reversed TiVs contribute to significant lift surges or drops by generating large low-pressure cores near the wing. Second, the TiVs play a part in attenuating lift fluctuations through enhanced downwash or upwash, formation of an arch vortex and distortion of vortical structure around the wing corners. The second effect outweighs the first, resulting in smaller transient lift changes on the finite wing compared with the two-dimensional wing. We also show that flying above a positive gust vortex or flying below a negative one can mitigate lift fluctuations during encounters. The current findings provide potential guidance on how TiV dynamics and wing positions could be leveraged to alleviate large transient lift fluctuations experienced by finite wings in severe gust conditions.

Key words: vortex dynamics, vortex interactions, separated flows

© The Author(s), 2026. Published by Cambridge University Press. This is an Open Access article, distributed under the terms of the Creative Commons Attribution licence (https://creativecommons.org/licenses/by/4.0/), which permits unrestricted re-use, distribution and reproduction, provided the original article is properly cited.

https://doi.org/10.1017/jfm.2026.11728 Published online by Cambridge University Press

1. Introduction

Strong gust encounters present a substantial challenge in aviation because of their time-variant, transient dynamics with strong nonlinearity. Such gust encounters exert large unsteady aerodynamic loads on wings, negatively impacting flight stability and aircraft structures (Fuller 1995; Wu, Cao & Ismail 2019; Jones, Cetiner & Smith 2022). Especially for small-scale air vehicles, such as drones, the relative scale of gust disturbances can be disproportionally large, a consequence of the small size and low cruise velocity associated with these vehicles (Mueller & DeLaurier 2003; Jones *et al.* 2022). For instance, during low-speed manoeuvre operations of small-scale aircraft, such as takeoff or landing in confined urban environments, the relative strength of gusts can be significantly high. Typically, when the gust ratio G – the ratio between characteristic gust velocity and cruise velocity – exceeds 1, the aerodynamic environment is considered unflyable. When $G > 1$, the dynamics of the flow is referred to as extreme aerodynamics (Fukami & Taira 2023; Lopez-Doriga, Jones & Taira 2026; Taira 2026). To enable the use of small-scale aircraft for transportation, agriculture and search-and-rescue (Cai, Dias & Seneviratne 2014; Hassanalian & Abdelkefi 2017; Ahirwar *et al.* 2019; Mishra *et al.* 2020) during adverse weather, it is crucial to advance our understanding of extreme aerodynamics.

To address this issue, past literature studying unsteady aerodynamics associated with gust–wing interactions provides valuable insights. Early efforts examined the aerodynamics of gust–wing interaction using linear thin aerofoil theory (Press & Mazelsky 1954; Horlock 1968; Goldstein & Atassi 1976). They treated gusts as weak perturbations, assuming attached flows. For instance, Atassi (1984) derived lift formulas for a thin aerofoil with small camber at a low angle of attack subjected to a vertical gust, incorporating the effect of the distortion of the gust structure. Their theoretical analysis was later shown to be in good agreement with experimental results (Cordes *et al.* 2017).

More recent studies have explored gust ratios in the range of $0 < G \lesssim 1$, where massive flow separation occurs around wings. These studies analysed vortex interactions and aerodynamic force responses for various types of gust encounters (Jones & Cetiner 2021), including transverse gusts (Wang *et al.* 2024), streamwise gusts (Ma *et al.* 2021) and vortex gusts (Martínez-Muriel & Flores 2020). For instance, Peng & Gregory (2017) experimentally examined load distributions on a two-dimensional (2-D) wing during vortex gust encounters in the context of blade–vortex interactions. Furthermore, Herrmann *et al.* (2022) designed a closed-loop controller using an actuated trailing-edge flap on an aerofoil to attenuate lift fluctuation during vortical gust encounters. Building upon this body of work, extreme vortex-gust–wing interactions with $G \gtrsim 1$ were recently investigated at a Reynolds number of 100 by Fukami & Taira (2023) and Fukami, Nakao & Taira (2024). They observed massive flow separation with high levels of transient lift change and developed a lift-attenuation strategy based on a low-order manifold around which the extreme dynamics evolves.

While the previously mentioned studies mainly focus on 2-D or spanwise periodic wings in the absence of tip vortices (TiVs), there exists some work that examined gust encounters by a finite wing. Barnes & Visbal (2018*a*,*b*) investigated the evolution of boundary layers and the force load on a finite wing during vortex-gust encounters. Control strategies, such as passive twist wingtips, for force load attenuation on a finite wing during vertical gust encounters were also proposed by Guo, Espinosa De Los Monteros & Liu (2015) and He *et al.* (2021). However, their work is primarily centred around $G \lesssim 1$ at a low angle of attack. Therefore, building a foundational understanding of gust–finite-wing interactions in a regime of $G \gtrsim 1$ is critical to further advancing the field of extreme aerodynamics.

https://doi.org/10.1017/jfm.2026.11728 Published online by Cambridge University Press

This study aims to elucidate the aerodynamics of extreme finite-wing–vortex-gust interactions at a Reynolds number of 600. The Reynolds number is sufficiently high to trigger massive flow separation, yet still low enough to preserve a laminar flow. Note that the core vortical structures observed in massively separated flows maintain topological similarities between low- and high-Reynolds-number regimes (Hunt *et al.* 1978; Dallmann 1988; Délery 2001), while the varying scales of vortical structures present at high Reynolds numbers significantly complicate flow analysis, especially without an understanding of large-scale vortex behaviour. Furthermore, for extreme aerodynamics, there is a disparity between the advective time scale and the viscous time scale, with the former being considerably smaller than the latter (Taira 2026). As such, the vortex core dynamics is similar across a range of Reynolds numbers. Large-scale vortical similarities between laminar and turbulent extreme aerodynamics are also discussed in a recent study (Odaka, Lopez-Doriga & Taira 2026). By exploring the large-scale vortical dynamics in the absence of turbulence, this work aims to establish a foundation for understanding extreme gust encounters by finite wings, setting a stepping stone for future investigations at higher Reynolds numbers.

In the present study, we perform direct numerical simulations of extreme vortex gust encounters by a square wing and analyse the complex interplay between flow structures, including a gust vortex, wing-surface separation and TiVs. Moreover, we identify vortical structures that serve prominent roles in aerodynamics. The rest of the paper is structured as follows. The computational set-up for an extreme vortex-gust encounter by a square wing is described in § 2. We present the vortex dynamics of the encounters and identify primary vortical structures responsible for the high lift changes in § 3. We also discuss the attenuation of lift variations due to TiV dynamics and wing positions against an impacting gust vortex, providing insights into mitigation strategies of the transient lift fluctuations. Concluding remarks are offered in § 4.

2. Problem set-up

We analyse flows around a NACA0015 finite wing impacted by a vortex gust, as presented in figure 1(*a*). The vortex gust is modelled as a spanwise-oriented vortex column with the circumferential velocity profile of a Taylor vortex (Taylor 1918):

$$u_\theta = u_{\theta,max}\frac{r}{R}\exp\left[\frac{1}{2}\left(1-\frac{r^2}{R^2}\right)\right], \tag{2.1}$$

where $u_{\theta,max}$ is the maximum rotational velocity at radius $r = R$. This vortex gust is characterised by the gust ratio

$$G \equiv u_{\theta,max}/u_\infty, \tag{2.2}$$

where u_∞ is the free-stream velocity. The circumferential velocity profile and the spanwise vorticity distribution are provided in figure 1(*b*).

We consider a square wing (semi-aspect ratio $sAR = 0.5$) with a straight-cut wingtip at an angle of attack of $\alpha = 14°$ and a chord-based Reynolds number of $Re = u_\infty c/\nu = 600$, where c is the chord length and ν is the kinematic viscosity. The aspect ratio is selected to effectively study tip effects, while the angle of attack is chosen to ensure a leading-edge flow separation is present for the undisturbed flow. We selected the Reynolds number to examine large-scale vortical dynamics in the absence of turbulence. The steady baseline (undisturbed) flow imposes a lift of $C_{L,base} = 0.22$, where the lift coefficient is defined as $C_L \equiv F_L/(1/2)\rho u_\infty^2 bc$. Here, F_L is the y component of the force load on the wing, ρ is density and b is the half-span length.

https://doi.org/10.1017/jfm.2026.11728 Published online by Cambridge University Press

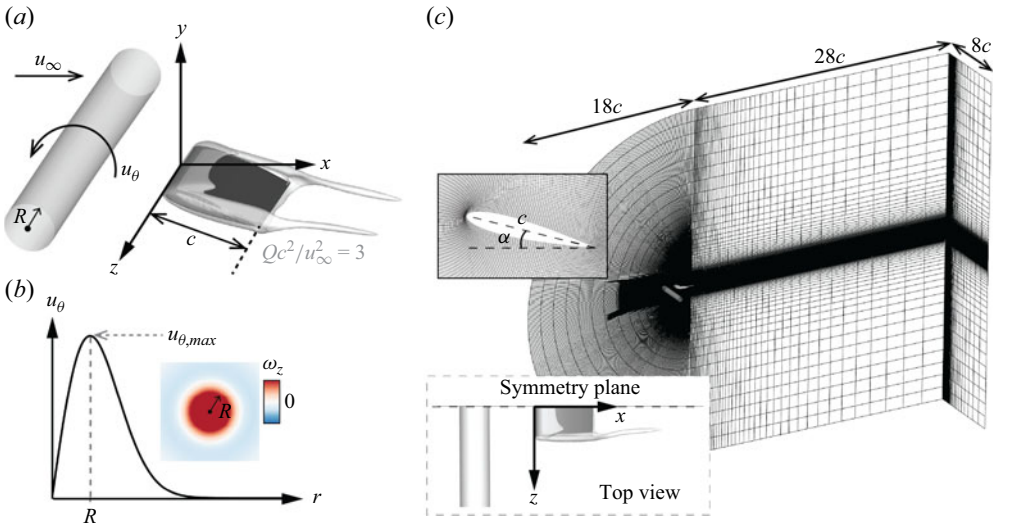


Figure 1. (*a*) A NACA0015 square wing encountering a gust vortex modelled as a Taylor vortex. The *Q*-criterion isosurface is shown. (*b*) Circumferential velocity profile and spanwise vorticity distribution of a Taylor vortex with a positive orientation. (*c*) Computational domain and discretisation.

We perform direct numerical simulations with the compressible flow solver CharLES (Brès *et al.* 2017), a finite-volume solver with second-order and third-order accuracy in space and time, respectively. The Mach number $u_\infty/a_\infty = 0.1$ is used to minimise compressible flow effects. The computational domain is shown in figure 1(*c*), where we respectively define x, y and z as the streamwise, vertical and spanwise coordinates with the leading edge of the wing root at the origin (0, 0, 0). We impose a Dirichlet boundary condition of $u_\infty/a_\infty = 0.1$ at the inlet and farfield boundaries, an adiabatic wall boundary condition at the wing surface and a sponge boundary condition at the outlet boundary. Along the $z/c = 0$ plane (wing root), we prescribe a symmetry boundary condition. The time step is selected such that the local Courant number is less than 1 throughout the entire computational domain. The present simulation is verified through a grid convergence study and validated with the lift coefficient for similar $sAR = 0.5$ and $sAR = 2$ wings reported in Zhang *et al.* (2020) and Ribeiro *et al.* (2023), as detailed in Appendix B.

We select four values of gust ratios $G = \{-1.2, -3, 1.2, 3\}$ with a fixed gust radius of $R/c = 0.25$. We introduce the gust vortex at a fixed streamwise location of $x_0/c = -3$ and varied vertical positions of $y_0/c = \{-0.25, 0, 0.25\}$ in the fully converged undisturbed flow and allow it to convect with the free stream. We define a reference time $\tau = u_\infty t/c$, such that $\tau = 0$ corresponds to the time at which the centre of the vortex column would reach the leading edge if there were no diffusion or interaction between the gust and any other flow structures. For comparison, we also simulate extreme vortex gust encounters with a NACA0015 2-D wing over a strictly 2-D domain, where we use the same free-stream and vortex conditions as in the square-wing case.

3. Results

Let us begin by examining the lift response experienced by the wings encountering an extreme gust vortex initially introduced at $(x_0/c, y_0/c) = (-3, 0)$. The time traces of lift coefficients for $G = \{-1.2, -3, 1.2, 3\}$ are shown in figure 2, where dashed and solid lines represent the 2-D and square wings, respectively. The baseline flow around the 2-D

https://doi.org/10.1017/jfm.2026.11728 Published online by Cambridge University Press

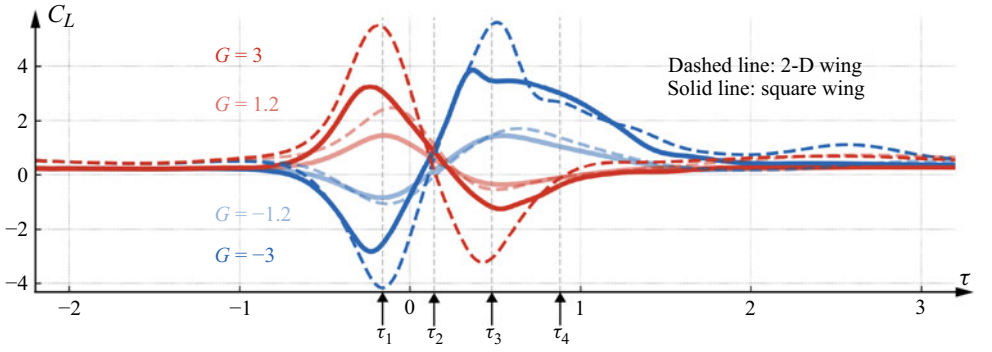


Figure 2. Lift history for the 2-D (dashed line) and square (solid line) wings with $G = \{-1.2, -3, 1.2, 3\}$. Representative temporal instances are indicated with $\tau = \tau_1$, τ_2, τ_3 and τ_4.

wing is unsteady with $\bar{C}_{L,base} = 0.49$, while the baseline flow around the square wing is steady with $C_{L,base} = 0.22$. Note that the unsteady unperturbed flow for the 2-D wing can capture the unsteady flow physics even from the start of the gust encounter. Although the baseline flow for the 2-D wing exhibits unsteady wake, we confirm that the timing of the gust encounter with respect to the oscillation in the baseline lift causes no significant difference in the transient lift during the extreme encounters, similar to a recent study with an infinite-span wing (Fukami, Smith & Taira 2025). This is because the large lift fluctuation due to the extreme encounters is much more significant than the lift fluctuation of the undisturbed case.

In the 2-D case, the maximum lift load in the vortex encounters exceeds five times the baseline value for $G = 1.2$ and eleven times for $G = 3$, as shown in figure 2. Compared with the 2-D wing, the square wing experiences notably lower lift spikes. However, despite this reduction, the finite wing still undergoes substantial lift fluctuations. In the following sections, we explain what vortex dynamics are responsible for the large lift changes and what the key three-dimensional dynamics are that cause the reduced lift response compared with the 2-D wing.

3.1. *Vortex encounters by the 2-D wing*

We analyse the flow dynamics during the extreme vortex gust encounters by the 2-D wing with $y_0/c = 0$. The evolutions of spanwise vorticity ω_z are shown in figure 3 at the four temporal instances from $\tau = \tau_1$ to τ_4 noted in figure 2. For positive vortex cases ($G = 1.2$ and 3 in figure 3), the increasing effective angle of attack due to the incoming gust vortex promotes vorticity generation from the leading edge, forming a large leading-edge vortex (LEV) above the wing. Furthermore, the approaching gust vortex increases the wall-normal velocity gradient on the bottom surface of the wing, increasing the vorticity contained within the boundary layer. The attached lower boundary layer with an increased level of vorticity flux on the bottom surface, coupled with a separated upper boundary layer, leads to the formation of a trailing-edge vortex (TEV). Accordingly, the lift peak rises to 2.47 and 5.49 for $G = 1.2$ and $G = 3$, respectively.

Focusing our attention on times $\tau = \tau_2$ and τ_3 for $G = 1.2$ and 3, the gust vortex is significantly deformed when it impinges upon the leading edge of the wing. The lower part of the gust vortex merges with the boundary layer on the bottom surface of the wing, while the upper part of the gust vortex convects upward and downstream, forming a vortex-pair-like structure including the LEV. By $\tau = \tau_3$, the LEV separates from the wing, causing the wing to lose the major lift-generating structures while the negative-lift-contributing

https://doi.org/10.1017/jfm.2026.11728 Published online by Cambridge University Press

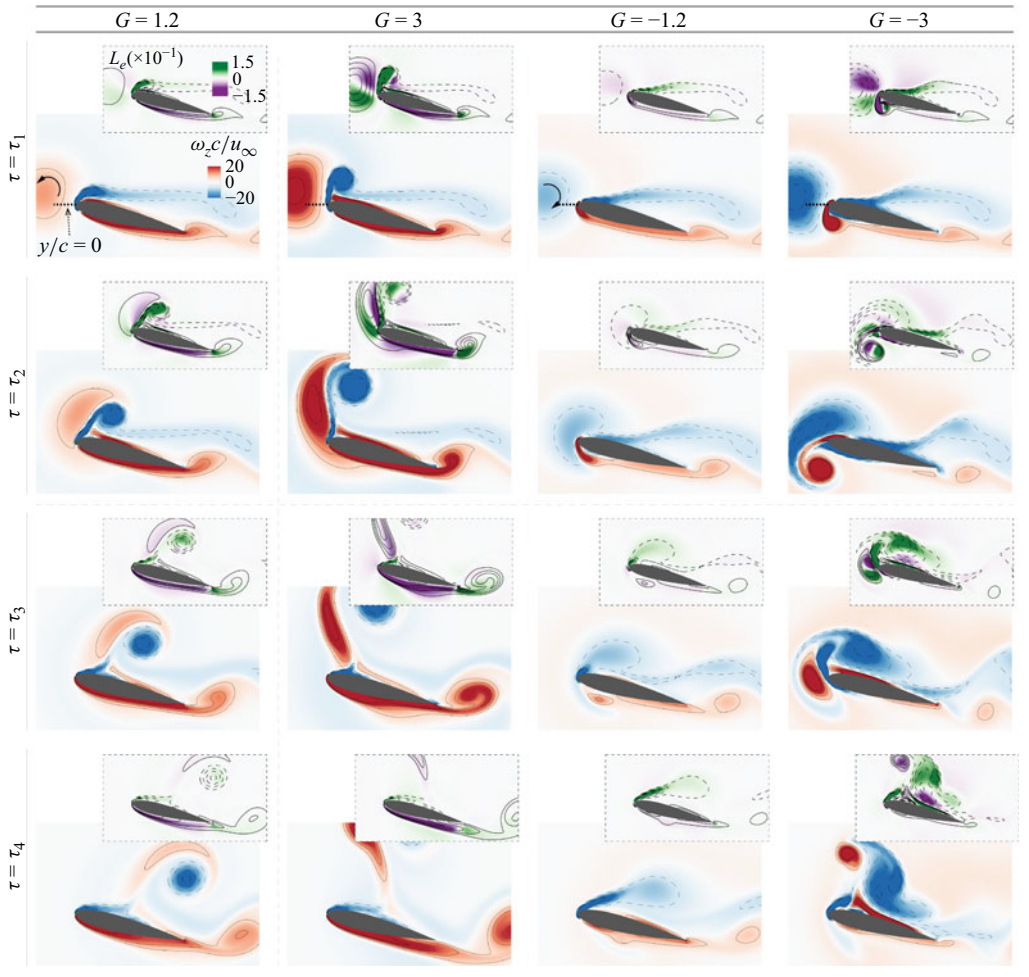


Figure 3. Snapshots of spanwise vorticity ω_z for the 2-D wing with $G = \{-1.2, -3, 1.2, 3\}$ at four temporal instances $\tau = \tau_1$ to τ_4 noted in figure 2. Lift elements L_e (green and purple contours) with lined contours of ω_z are inset at the top right of each subplot.

structures on the lower surface remain – the lift coefficient peak drops to -3.22 for $G = 3$. By $\tau = \tau_4$, the leading-edge shear layer gradually starts reforming, restoring the baseline flow state.

The evolutions of 2-D, negative vortex cases are similar to those of the positive vortex cases, but with a reversal in the direction of the gust-induced velocity. As shown for $G = -1.2$ at $\tau = \tau_1$ in figure 3, vertically downward velocity from the approaching gust vortex delays separation above the wing while vorticity generation is promoted below the wing although it does not grow enough to form an LEV. For $G = -3$, the downward velocity by the approaching gust vortex is so strong that an LEV develops beneath the wing, causing the lift coefficient C_L to drop below -4.

For both $G = -1.2$ and -3, the gust vortex merges with the leading-edge shear layer on the upper surface around $\tau = \tau_2$. Moreover, for $G = -3$, the LEV forming below the wing induces counter-rotating vorticity between itself and the wing, generating another vortical structure, as observed at $\tau = \tau_2$ in figure 3. This structure grows along with the LEV until it disrupts the vortical sheet feeding the LEV, resembling the dynamics

https://doi.org/10.1017/jfm.2026.11728 Published online by Cambridge University Press

observed around a revolving wing (Garmann & Visbal 2014). Afterward, this opposite-signed vortical structure rolls up over the leading edge, eventually forming a secondary LEV on the top side of the wing, as seen at $\tau = \tau_3$ and τ_4.

To quantify the contribution of vortical structures to lift, we use force element analysis (Chang 1992; Menon & Mittal 2021), a method to identify flow structures responsible for load generation on the wing. We derive an auxiliary potential ϕ_y under a boundary condition of $-\boldsymbol{n} \cdot \boldsymbol{\nabla}\phi_y = \boldsymbol{n} \cdot \boldsymbol{e}_y$ on the wing surface, where $\boldsymbol{e_y}$ is the unit vector in the y direction. By integrating the inner product of the Navier–Stokes equations with $\boldsymbol{\nabla}\phi_y$ over the fluid domain, we can express the lift force as

$$F_L = \int_V \boldsymbol{\omega} \times \boldsymbol{u} \cdot \boldsymbol{\nabla}\phi_y \, \mathrm{d}V + \frac{1}{Re} \int_S \boldsymbol{\omega} \times \boldsymbol{n} \cdot \left(\boldsymbol{\nabla}\phi_y + \boldsymbol{e}_y\right) \, \mathrm{d}S. \tag{3.1}$$

The first integrand represents volume lift elements while the second integrand represents surface lift elements. For the current flows at $Re = 600$, the volume lift elements have dominant contributions to lift force compared with the surface elements (Ribeiro *et al.* 2023). We hereafter refer to the volume lift element as lift element L_e.

The lift element plot is inset at the top right of each subplot in figure 3, where green and purple contours correspond to lift-increasing and lift-decreasing elements, respectively. For the positive vortex cases, the LEV is the prominent contributor to positive lift, while the boundary layer on the lower surface and the gust vortex merged with it primarily yield negative lift. For instance, the lift contribution from the LEV at $\tau = \tau_1$ for $G = 3$ totals 4.63, where the lift elements with $L_e \geqslant 0.015$ inside the vortex are integrated and scaled by $(1/2)\rho u_\infty^2 c$. In contrast, for the negative gust vortex cases, the LEV and shear layer below the wing mainly contribute to negative lift, whereas the gust vortex merged with the shear layer on the top surface and the secondary LEV predominantly generate positive lift; e.g. at $\tau = \tau_1$ for $G = -3$, the LEV below the wing accounts for a total negative-lift contribution of -2.63 (integration of the lift elements with $L_e \leqslant -0.015$ inside the vortex). In the next subsection, we explore the effects of the wing being finite (in the spanwise direction) on the vortex dynamics and lift fluctuations in extreme vortex gust encounters.

3.2. *Positive vortex encounters by the square wing*

Let us examine the three-dimensional vortex gust encounters by the square wing, focusing on vortical structures responsible for large lift variation and its attenuation compared with the 2-D wing. The temporal evolution of vortical structures for the positive gust vortex cases with $y_0/c = 0$ is presented in figure 4, where we visualise a Q-criterion isosurface in grey and three representative vortex lines in black, aqua and orange at each instance. Note that the plotted vortex lines are shown to facilitate describing the details of vortical structures, and lines in the same colour do not necessarily represent the same structures being tracked over time. Each panel also presents spanwise slices of lift element L_e (coloured contour) and ω_z (lined contour) along the root $z/c = 0$ and near the wingtip $z/c = 0.48$ on the right.

We first note that the vertical position of the positive gust vortex at impact is lower for the square-wing case than for the 2-D wing case. This is attributed to a lower upward velocity upstream of the leading edge of the wing, induced by the bound circulation around the square wing, compared with the 2-D wing. This comparison of the vertical position of the gust vortex can be seen for both $G = 1.2$ and 3 cases in gust position relative to $y/c = 0$ at $\tau = \tau_1$ in figure 3 and the spanwise slices in figure 4.

Let us discuss the effects of TiVs, some of the primary vortices present in flows around the square wing but absent in the 2-D wing cases. When the gust vortex is approaching

https://doi.org/10.1017/jfm.2026.11728 Published online by Cambridge University Press

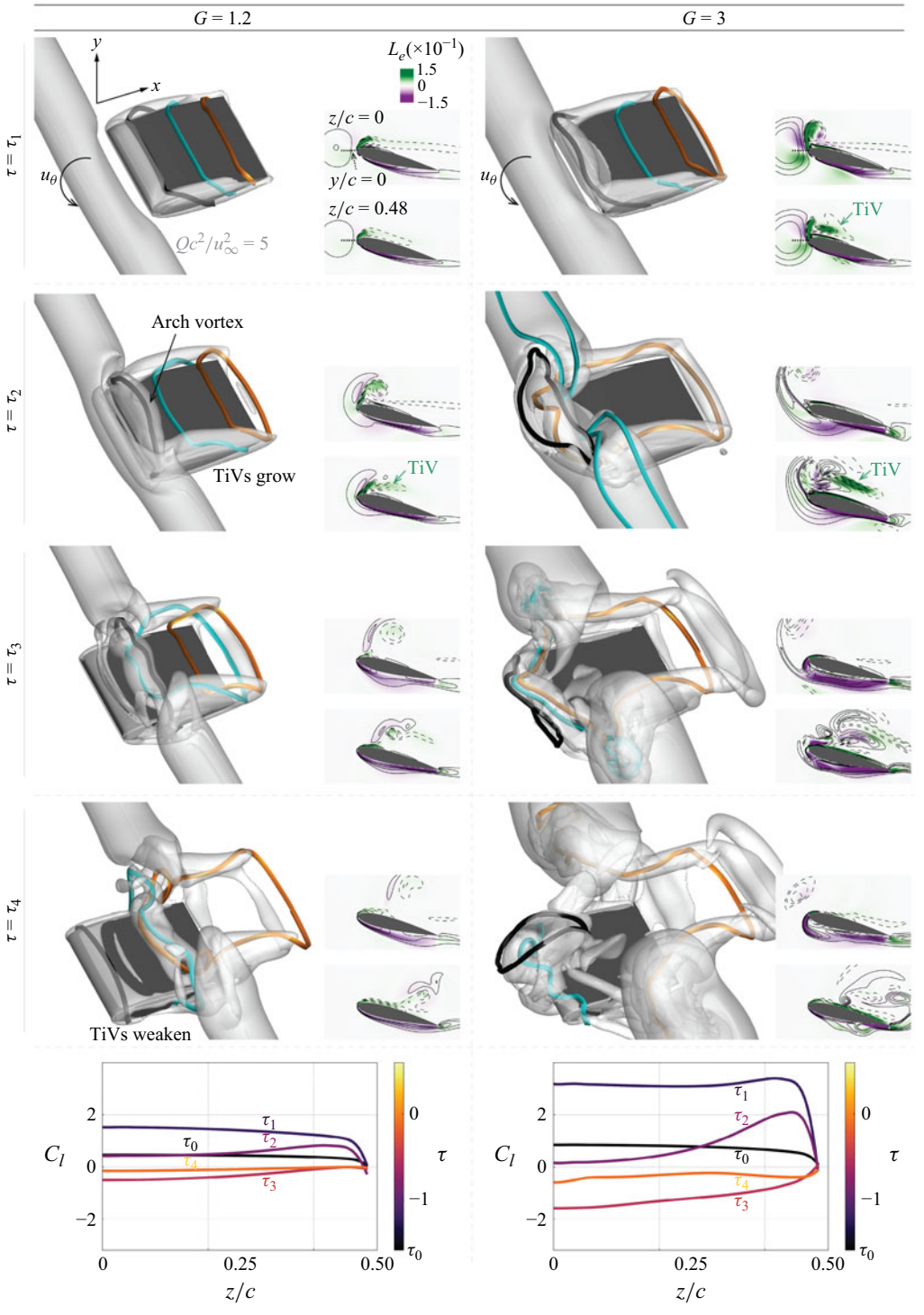


Figure 4. Top-port views for the square-wing cases with $G = 1.2$ and 3 at the four temporal instances noted in figure 2. The Q-criterion isosurface is shown in grey with three representative vortex lines coloured in black, aqua and orange. Spanwise slices of lift elements L_e (colour contours) with ω_z (line contours) along the root $z/c = 0$ and near the tip $z/c = 0.48$ are shown on the right of each subplot. Sectional lift distributions at $\tau_0 = -0.6$ and $\tau = \tau_1$ to τ_4 are presented at the bottom.

https://doi.org/10.1017/jfm.2026.11728 Published online by Cambridge University Press

the wing, the TiVs grow in size and strength, particularly towards the leading edge. This occurs because the enhanced upward velocity from the incoming gust vortex increases the pressure difference between the upper and lower surfaces of the wing. The strengthened TiVs locally produce enhanced downwash, as indicated in a larger sectional lift drop near the tip at $\tau = \tau_1$ than $\tau = \tau_0$ in the last row of figure 4, which displays the time evolution of sectional lift distribution at $\tau_0 = -0.6$ and $\tau = \tau_1$ to τ_4. An additional discussion on the enhanced downwash is provided in Appendix A. After the gust vortex passes the wing, its vertical velocity around the wing directs downward. This reduces the pressure difference between both sides of the wing, weakening the TiVs. The TiV evolution can be seen in figure 4, where the TiVs strengthen as the gust vortex approaches the wing and weaken after it moves past the wing.

Next, let us examine how the vortices form and interact with each other around the finite wing. As observed at τ_1 in figure 4, the LEV, TiVs and boundary layer on the wing bottom form a closed loop of a vortex line. By $\tau = \tau_2$, the LEV around the tips is anchored to the wing corners, transforming into an arch vortex. For $G = 1.2$ at $\tau = \tau_3$, arch vortices convect above the wing, with their legs connecting to the TiVs (the vortex line in aqua) or the boundary layer on the bottom surface (the vortex line in black). Over time, the arch vortices convect downstream, exhibiting kinks near the tip ($\tau = \tau_4$).

For $G = 3$ at $\tau = \tau_2$, part of the LEV becomes connected with the upper portion of the gust vortex, forming a vortex loop (the vortex line in black). Another part of the LEV forms a loop with the TEV (the vortex line in orange). The aqua-coloured vortex line depicts part of the gust vortex connecting to vortical structures that have opposite-sign spanwise vorticity outside of the gust vortex core. At $\tau = \tau_3$, the LEV connects to the gust vortex (black), the boundary layer below the wing (aqua) and the TEV (orange). By $\tau = \tau_4$, the vortical structure represented by the vortex line in black distorts around the arch vortex.

Let us turn our attention to the vortical structures responsible for the large lift change through the lens of lift elements in figure 4. We find similarities with the 2-D wing cases. The LEV remains the primary contributor to positive lift, while the boundary layer on the bottom surface and the gust vortex merged with it play a dominant role in negative lift; e.g. the lift elements of the LEV total 1.91 at $\tau = \tau_1$, where the volume integral of lift elements with $L_e \geqslant 0.015$ inside the vortex is performed and normalised by $(1/2)\rho u_\infty^2 bc$.

However, in the finite-wing case, another prominent source of positive lift emerges: the TiVs, particularly notable at $\tau = \tau_1$ and τ_2. While the TiVs cause sectional lift reduction due to their local downwash, the TiVs, strongly amplified by the impacting gust vortex, generate large low-pressure cores above the wing, enhancing their local contribution to vortex lift (Lee *et al.* 2012; Smith & Taira 2024). Specifically, at $z/c = 0.48$, the sectional lift attributed to the TiV for $G = 3$ is 0.89, which is nearly three-quarters of that by the LEV ($= 1.24$), where we integrate lift elements with $L_e \geqslant 0.015$ inside each vortex along the spanwise slice. Although the lift contribution of the TiVs is pronounced only around the tip, their contribution to the total lift is 0.34 at $\tau = \tau_1$, which is over 10 % of it. The positive-lift effect of the TiVs is also observed in the sectional lift distribution visualised in figure 4, where, with the growth of the TiVs, the section lift has a positive peak near the wingtips, a trend particularly pronounced at $\tau = \tau_2$.

We further examine key three-dimensional vortex dynamics that attenuate lift fluctuation compared to the 2-D case. First, the effective angle of attack is reduced likely due to the enhanced downwash by the strengthened TiVs, decreasing positive lift around the first peak at $\tau = \tau_1$. Additionally, the formation of the arch vortex suppresses LEV development (Lee *et al.* 2012), further reducing positive lift. The arch vortex also plays a role in attenuating the negative peak at $\tau = \tau_3$ by keeping the LEV closer to the

https://doi.org/10.1017/jfm.2026.11728 Published online by Cambridge University Press

upper surface near the tips. Moreover, spanwise vorticity generation in the lower-surface boundary layer is suppressed around the wingtips while the gust vortex merging with the boundary layer distorts around the wing corners, leading to a decreased level of spanwise vorticity on the underside of the wing – and consequently, a reduction in negative-lift elements compared with the 2-D wing. This loss of negative-lift elements near the tips leads to an increasing trend in the sectional lift towards the wingtip, as seen particularly at $\tau = \tau_3$ in the last row of figure 4.

We therefore find two opposing effects of the TiVs on the large lift fluctuations induced by an extreme positive gust vortex. First, they contribute to positive lift by creating large low-pressure cores near the tips above the wing. Second, they attenuate the large lift surge and drop, due to enhancing downwash with their growth and forming arch vortices. The second effect, combined with reduced spanwise vorticity generation in the lower-surface boundary layer and the distortion of the gust vortex around the tips, dominates the first, resulting in the finite wing undergoing smaller lift fluctuations than the 2-D wing. This suggests that further promoting TiVs during interaction with a positive gust vortex could lead to a greater attenuation of large transient lift fluctuations.

3.3. *Negative vortex encounters by the square wing*

Let us analyse the negative gust vortex cases, shown in figure 5. First, the evolution of the TiVs follows an opposite trend to that observed in the positive gust vortex cases. Specifically, TiVs first weaken and even reverse orientation, particularly near the leading edge, because the downward velocity of the approaching gust vortex applies higher pressure on the top surface and temporarily inverts the pressure and suction effects on the wing. Note that the reversed TiVs induce local upwash effects, as can be seen in the sectional lift at $\tau = \tau_1$ in the last row of figure 5, where the sectional lift exhibits a sharp increase near the wingtip. An additional discussion on the upwash is presented in Appendix A. Once the gust vortex passes, TiVs regain strength in their original orientations, affected by the upward velocity from the gust vortex.

This evolution is observed in the Q-criterion isosurface in figure 5. At $\tau = \tau_1$, the reversed TiVs around the leading edge are visible, while the TiVs near the trailing edge are too weak to be captured by the isosurface. By $\tau = \tau_4$, the TiVs recover in the original orientation, particularly near the leading edge. The sectional lift plot in the last row of figure 5 also reveals the effects of the TiV dynamics. Due to the reversed TiVs, the sectional lift exhibits an increasing trend towards the tips at $\tau = \tau_1$ for both $G = -1.2$ and -3. Around $\tau = \tau_3$, the sectional lift trend shifts back to a decreasing one, owing to a recovery of the TiVs in the original orientation.

We now analyse the three-dimensional interactions and connections between vortical structures. Similar to the positive gust vortex cases but on the other side of the wing, the LEV and TiVs interconnect and form arch vortices below the wing, as seen at $\tau = \tau_2$ for both $G = -1.2$ and -3 in figure 5. For $G = -1.2$, the vortices advect downstream along the wing over time, exhibiting kinks around the quarter spans on the upper surface at $\tau = \tau_4$ affected by the recovered TiVs.

For $G = -3$, the legs of the arch vortices in the inboard region are pushed towards and localised around the root by $\tau = \tau_3$ (the vortex line in black), while the legs near the wingtips attach to the bottom surface of the wing (the vortex line in aqua). Furthermore, vortex lines connecting the TEV and reversed TiVs link to the gust vortex (the vortex line in orange). By $\tau = \tau_4$, the arch vortex localised inboard is further pushed towards the root and stretched into a hairpin vortex. The formation of this stretched hairpin vortex disrupts the redevelopment of the leading-edge shear layer on the upper surface, as seen in the

https://doi.org/10.1017/jfm.2026.11728 Published online by Cambridge University Press

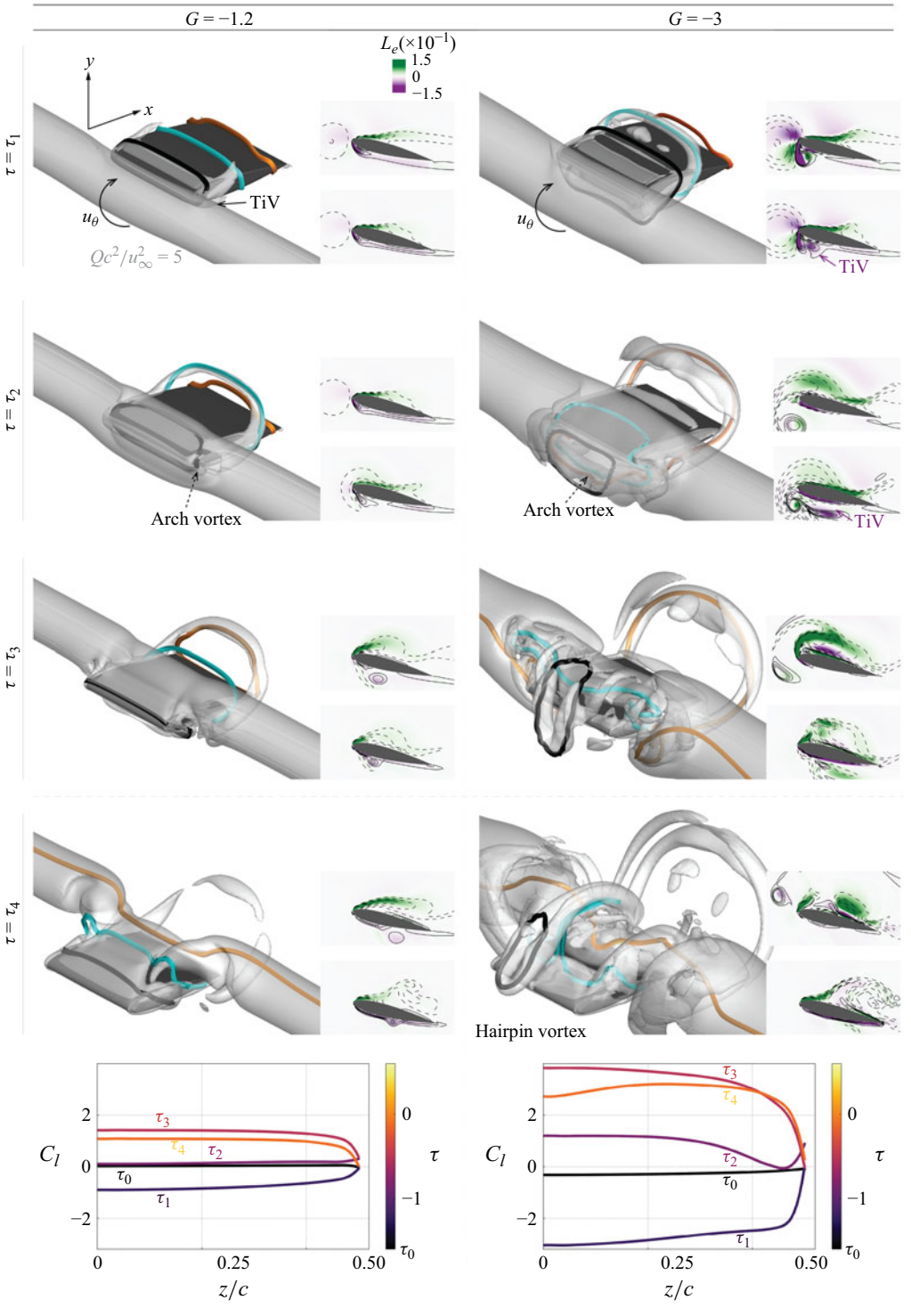


Figure 5. Same isosurface, spanwise slices and sectional lift distributions as in figure 4 for $G = -1.2$ and -3.

https://doi.org/10.1017/jfm.2026.11728 Published online by Cambridge University Press

spanwise slice at the root in figure 5. After $\tau = \tau_4$, the stretched hairpin vortex convects above the wing, although the subsequent evolution of the vortices is not shown in figure 5.

Next, let us identify the dominant vortical structures responsible for the large lift fluctuations through lift element analysis in figure 5. Similar to the 2-D wing cases, the LEV and shear layer beneath the wing primarily drive the first negative peak at $\tau = \tau_1$, while the gust vortex merged with the leading-edge shear layer on the upper surface is the main contributor to the positive-lift peak at $\tau = \tau_3$. For the square-wing cases, the reversed TiVs also play a crucial role in negative lift generation by creating low-pressure cores below the wing. This effect is particularly visible for $G = -3$ at $\tau = \tau_1$ and τ_2, as shown in the lift element visualisations in figure 5, acting in the opposite manner to the strengthened TiVs in the positive vortex cases. The negative spike in the section lift for $G = -3$ at $\tau = \tau_2$ in the last row of figure 5 is also a consequence of the lift-decreasing effect by the low-pressure cores of the reversed TiVs.

Key structures that contribute to the attenuated lift response compared with the 2-D wing can also be uncovered. The first, negative peak is mitigated likely because of the upwash effects induced by the reversed TiVs. For the attenuation of the positive peak, there appear to be two main mechanisms. First, the arch vortex below the wing decreases lift by positioning the low-pressure regions closer to the bottom surface near the tips. Second, the positive lift attributed to the gust vortex merged with the leading-edge shear layer on the top surface is reduced particularly near the wingtips. This is because coherent spanwise vorticity of the gust vortex is partially lost as the gust vortex distorts around the wing corners, coupled with suppressed shear-layer development near the tips, as shown in figure 5.

We thus find two opposing ways that the finite wing affects the lift fluctuations for negative gust vortex cases: (i) the TiVs, which are low-pressure cores, develop below the wing through interaction with an impacting gust vortex, contributing to initial, large lift drop; (ii) the lift drop and surge are attenuated through the three-dimensional vortex dynamics such as the reversed TiVs and the distortion of the impacting gust vortex around the wing corners. Reminiscent of the positive gust vortex cases, the second effect outweighs the first, causing the square wing to experience a smaller lift variation than the 2-D wing. These results suggest that further amplifying TiV evolution – intensifying TiVs in the opposite orientation to the baseline in response to a negative gust vortex – could enhance the attenuation of the large lift changes.

3.4. *Influence of gust vortex vertical position*

Let us study the effects of the relative height difference between the wing and the approaching gust vortex. We first present lift fluctuations experienced by the 2-D and square wings encountering a gust vortex introduced at different initial vertical positions. Next, we examine the vortex dynamics around the 2-D wing that contributes to the large lift changes for the varied vertical position cases. We further analyse the flows around the square wing and investigate the finite-wing effects on the lift variations.

Here, we compare the lift histories for the 2-D and square wings subjected to a gust vortex with $G = \pm 3$ introduced at different initial vertical positions $y_0/c = \{-0.25, 0, 0.25\}$, as shown in figure 6. For the positive gust vortex, the 2-D wing experiences the lowest lift fluctuation for the $y_0/c = -0.25$ case compared with the other two position cases, although the initial peak is slightly higher than that observed for the $y_0/c = 0.25$ case. Similarly, the square wing exhibits the lowest lift fluctuation for the $y_0/c = -0.25$ case. For example, the initial lift peak for the $y_0/c = -0.25$ case with the square wing is 1.67 while that for the $y_0/c = 0$ case is 2.70. For all three vertical

https://doi.org/10.1017/jfm.2026.11728 Published online by Cambridge University Press

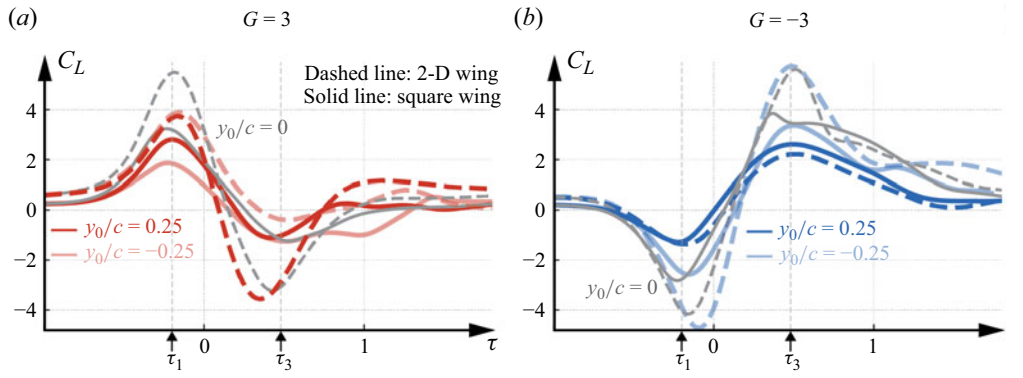


Figure 6. Lift history for the 2-D (dashed line) and square (solid line) wings encountering a gust vortex with $G = 3$ (*a*) and -3 (*b*) initially introduced at different vertical positions $y_0/c = \{-0.25, 0, 0.25\}$.

positions considered herein, the lift fluctuations are attenuated for the square wing compared with those for the 2-D wing.

For the negative gust vortex cases shown in figure 6(*b*), lift fluctuations are the lowest when both the 2-D and square wings fly beneath the gust vortex ($y_0/c = 0.25$) among the three vertical position cases considered. The 2-D wing experiences the largest lift fluctuation when the vortex is located at $y_0/c = -0.25$, whereas the square wing exhibits the largest fluctuation at $y_0/c = 0$. Notably, the lift peaks experienced by the square wing are reduced for all three examined vertical positions compared with the 2-D wing.

Let us shift our focus to the vortex dynamics around the 2-D wing, particularly for $y_0/c = \pm 0.25$, and its relation to the lift fluctuations. In figure 7, we visualise lift element L_e and spanwise vorticity ω_z for the 2-D wing with $y_0/c = \pm 0.25$ at $\tau = \tau_1$ and τ_3. Below the visualisation at $\tau = \tau_1$, we also show the contour lines of $\omega_z = -20$ for $G = 3$ and $\omega_z = 20$ for $G = -3$ to compare the size and position of the LEV between the cases with $y_0/c = 0$ and ± 0.25.

We examine the 2-D wing flying above the positive gust vortex $(G, y_0/c) = (3, -0.25)$, as shown in the first column of figure 7. As the gust vortex approaches the wing, a large LEV develops, similar to the positive gust vortex cases discussed in § 3.1. However, due to the lower vertical position of the gust vortex, the size and intensity of the LEV are weakened with its location shifted upstream compared with the $(G, y_0/c) = (3, 0)$ case. This weaker LEV results in a lower lift peak at $\tau = \tau_1$ than the $y_0/c = 0$ case. In addition, at $\tau = \tau_1$, a secondary vortical structure is induced between the LEV and the upper surface. By $\tau = \tau_3$, this secondary structure disrupts the vortical sheet feeding the LEV and rolls up around the leading edge. Furthermore, the gust vortex convects below the wing and disturbs the bottom-surface boundary layer, resulting in a reduction of vorticity contained in it, as seen in the bottom left panel of figure 7. This causes a loss of negative-lift elements on the lower surface, substantially diminishing the negative-lift peak, compared with the cases where the gust vortex is introduced higher; e.g. the negative-lift peak for the $(G, y_0/c) = (3, -0.25)$ case of the 2-D wing is -0.49 while that for the $(G, y_0/c) = (3, 0)$ case is -3.10.

Considering the 2-D wing flying below the positive gust vortex $(G, y_0/c) = (3, 0.25)$, as shown in the second column of figure 7, we observe similar vortex dynamics to the case with $(G, y_0/c) = (3, 0)$ presented in § 3.1. That is, at $\tau = \tau_1$, a large LEV forms on the upper surface while the approaching gust vortex increases the wall-normal velocity gradient in the bottom-surface boundary layer, enhancing vorticity generation. However,

https://doi.org/10.1017/jfm.2026.11728 Published online by Cambridge University Press

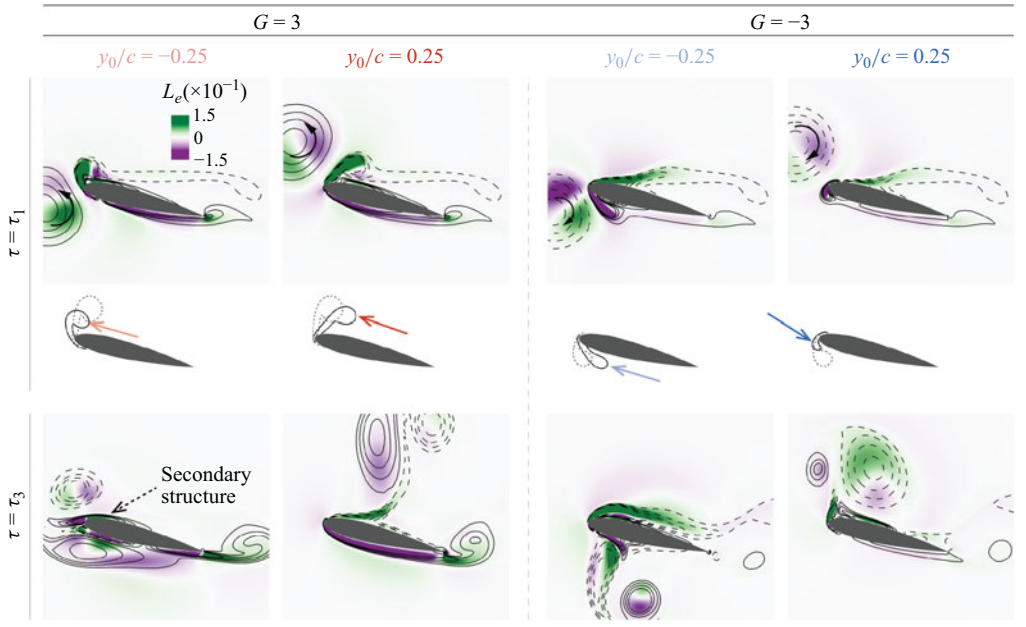


Figure 7. Lift element L_e (colour contour) and spanwise vorticity ω_z (line contour) for the 2-D wing cases of $G = \pm 3$ with $y_0/c = \pm 0.25$ at $\tau = \tau_1$ and τ_3. At $\tau = \tau_1$, contour lines of $\omega_z = -20$ for $G = 3$ and $\omega_z = 20$ for $G = -3$ are also visualised below to compare the LEV between $y_0/c = 0$ (dotted-line contour) and ± 0.25 (solid-line contour indicated by the coloured arrows).

compared with the $(G,\ y_0/c) = (3,\ 0)$ case, the LEV has a smaller growth with its location shifted downstream, resulting in a lower positive-lift peak. By $\tau = \tau_3$, the gust vortex convects downstream above the wing, forming a vortex-pair-like structure with the LEV. As a result, the wing loses most of the vortical structures contributing to positive lift. In contrast, vortical structures on the lower surface that contribute to negative lift persist, leading to a pronounced negative-lift peak.

Let us next focus on the negative vortex encounter with $(G,\ y_0/c) = (-3,\ -0.25)$ by the 2-D wing, as shown in the third column of figure 7. As the negative vortex approaches the wing, a strong LEV develops below the wing, leading to a significant negative-lift peak around $\tau = \tau_1$. Concurrently, a secondary vortical structure is induced between the LEV and the lower surface. However, as the gust vortex convects below the wing by $\tau = \tau_3$ forming a vortex-pair-like structure with the LEV, this secondary structure does not continue to grow, unlike the $(G,\ y_0/c) = (-3,\ 0)$ case discussed in § 3.1. On the top surface, the gust vortex induces a large wall-normal velocity gradient in the shear layer near the leading edge by $\tau = \tau_3$, generating a high level of vorticity, and, hence, large positive lift. This contributes to a significant second, positive-lift peak.

For the 2-D wing flying under the negative gust vortex $(G,\ y_0/c) = (-3,\ 0.25)$ as in the fourth column of figure 7, a smaller LEV develops below the wing at $\tau = \tau_1$, compared with the cases where the wing flies higher. As a result, the first lift peak for this case is the smallest among the three examined different vertical position cases. A secondary vortical structure induced between the LEV and the lower surface at $\tau = \tau_1$ rolls up around the leading edge by $\tau = \tau_3$, resembling the dynamics discussed for the $(G,\ y_0/c) = (-3,\ 0)$ case in § 3.1. However, the positive-lift elements associated with this secondary vortical structure around the leading edge are not as substantial as those

https://doi.org/10.1017/jfm.2026.11728 Published online by Cambridge University Press

observed in the $(G,\ y_0/c) = (-3,\ 0)$ case because of the smaller development of the LEV, resulting in a lower positive-lift peak than the $(G,\ y_0/c) = (-3,\ 0)$ case.

Thus, we find effective vertical positions of the 2-D wing to reduce large lift fluctuations against an impacting gust vortex; flying over the positive gust vortex and flying under the negative gust vortex. A similar trend is also observed in an experimental study by Peng & Gregory (2017). They reported that the force fluctuation during vortex-gust encounters by a 2-D wing with $|G| < 1$ at $Re = \mathcal{O}(10^5)$ in the context of blade–vortex interactions can be reduced when the aerofoil passes above a positive vortex or below a negative vortex.

We now turn our attention to the square-wing cases. Presented in figure 8 are the isosurfaces of Q-criterion and the spanwise slices of lift element L_e and spanwise vorticity ω_z along the root and near the tip for the square wing with $y_0/c = \pm 0.25$ at $\tau = \tau_1$ and τ_3.

For the $(G,\ y_0/c) = (3,\ -0.25)$ case, as shown in the first column of figure 8, an LEV develops on the upper surface at $\tau = \tau_1$, connecting to the strengthened TiVs around the wing corners. Similar to the discussion provided in § 3.2, the strengthened TiVs suppress the development of the LEV and induce enhanced downwash, particularly near the wingtips, resulting in a smaller first lift peak than in the 2-D wing case. By $\tau = \tau_3$, the LEV transforms into an arch vortex, with its legs pushed towards and positioned beneath the wing near the tips. The secondary vortical structure, which is induced between the LEV and the upper surface at $\tau = \tau_1$, rolls up around the leading edge and shifts to the underside of the wing, particularly near the wingtip. As in the 2-D case, the gust vortex, convecting below the wing, interacts with the bottom-surface boundary layer, weakening negative-lift elements on the lower surface. Moreover, as seen in the spanwise slice at $z/c = 0.48$ at $\tau = \tau_3$, the gust vortex loses some coherence in its spanwise structure near the tips, resulting in reduced negative-lift elements.

Let us next examine the square-wing case with $(G,\ y_0/c) = (3,\ 0.25)$, as shown in the second column of figure 8. As the gust vortex approaches the wing, a large LEV develops while the TiVs are amplified. As seen in the spanwise slice of the lift element visualisation along $z/c = 0.48$ at $\tau = \tau_1$, the TiVs contribute to positive lift near the tip due to their large low-pressure cores, similar to the cases discussed in § 3.2. Concurrently, the intensified TiVs locally induce enhanced downwash and suppress the development of the LEV, resulting in a lower initial lift peak compared with the 2-D wing case. By $\tau = \tau_3$, the gust vortex rolls up and lifts the arch vortex and TiVs significantly away from the wing, as visualised by the Q-criterion isosurface. Furthermore, spanwise vorticity generation in the bottom-surface boundary layer is suppressed near the tips, causing a loss of negative-lift elements, similar to the discussion provided in § 3.2. These finite-wing effects contribute to attenuating the negative-lift peak compared with the 2-D wing.

For the square wing encountering the negative gust vortex with $(G,\ y_0/c) = (-3,\ -0.25)$, as depicted in the third column of figure 8, a large LEV develops below the wing while the TiVs reverse orientation. The reversed TiVs locally induce upwash effects and suppress the LEV development near the tips, attenuating the first negative-lift peak compared with the 2-D wing case. Over time, the gust vortex rolls up the LEV and TiVs beneath the wing, disrupting the vortex sheet feeding the LEV, as visualised by the Q-criterion isosurface and spanwise slices at $\tau = \tau_3$. On the upper surface, the development of the leading-edge shear layer, enhanced by the impacting gust vortex as discussed for the 2-D wing case, weakens near the tips because the coherent structure of the gust vortex distorts around the wing corners. The weaker leading-edge shear layer results in reduced positive-lift elements, contributing to the damping of the second lift peak compared with the 2-D wing case.

For the square-wing case with $(G,\ y_0/c) = (-3,\ 0.25)$, as presented in the fourth column of figure 8, a smaller LEV forms below the wing at $\tau = \tau_1$ than in the cases where

https://doi.org/10.1017/jfm.2026.11728 Published online by Cambridge University Press

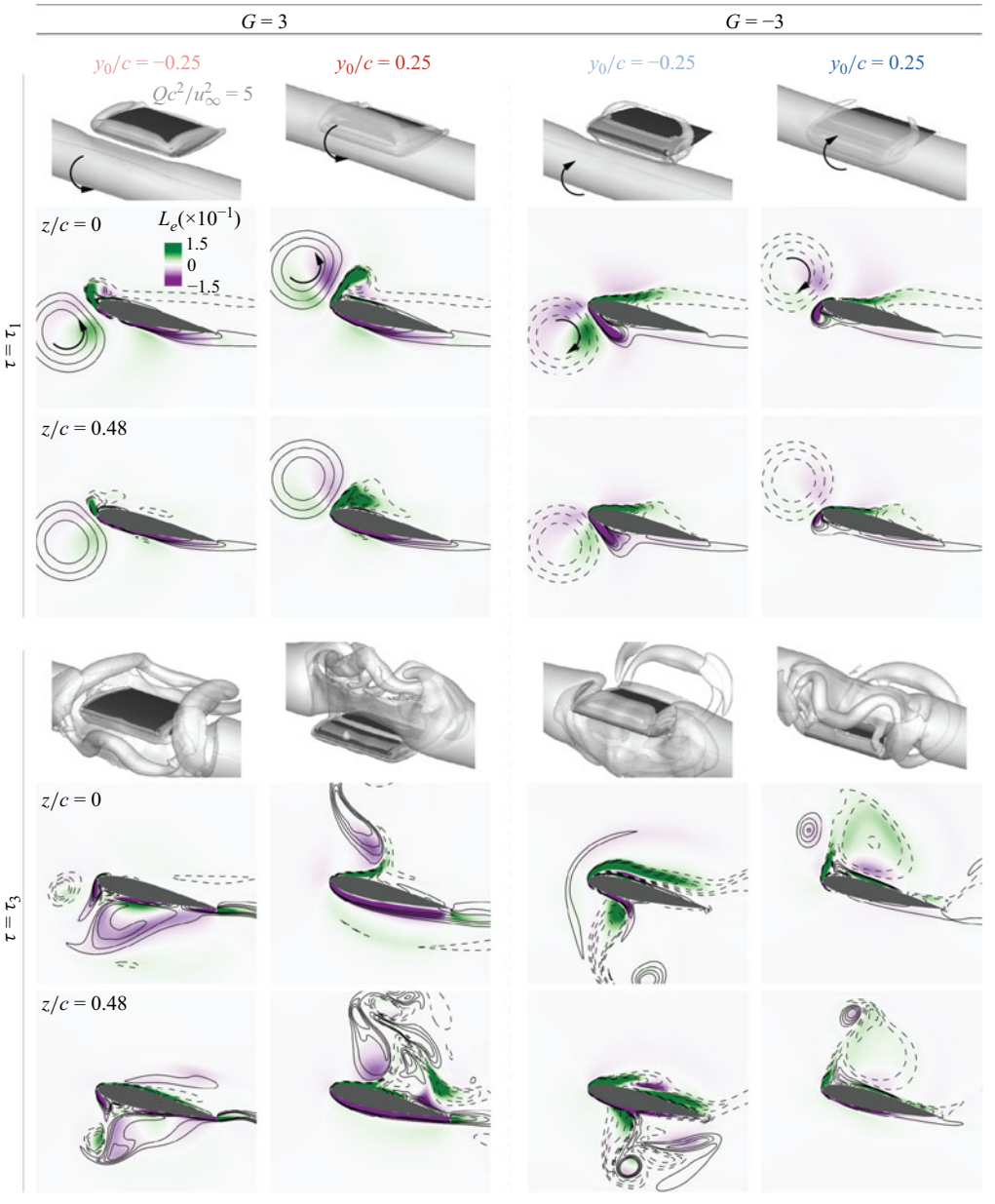


Figure 8. Isosurfaces of Q-criterion around the square wing and spanwise slices of L_e (colour contour) and ω_z (line contour) along the root and near the tip at $\tau = \tau_1$ and τ_3 for the $y_0/c = \pm 0.25$ cases.

the gust vortex is introduced lower. The reversed TiVs develop beneath the wing, inducing upwash effects, suppressing the development of the LEV, and thereby mitigating the first lift peak compared with the 2-D wing case. By $\tau = \tau_3$, the LEV forms an arch vortex, rolls up around the leading edge to the upper surface and separates from the wing with the legs connected to the TiVs. Similar to the 2-D case, the secondary vortical structure, which is induced between the LEV and the bottom surface at $\tau = \tau_1$, rolls up around the leading edge by $\tau = \tau_3$. As visualised in the spanwise slices at $\tau = \tau_3$, the positive-lift elements associated with this secondary vortical structure are reduced near the wingtips,

https://doi.org/10.1017/jfm.2026.11728 Published online by Cambridge University Press

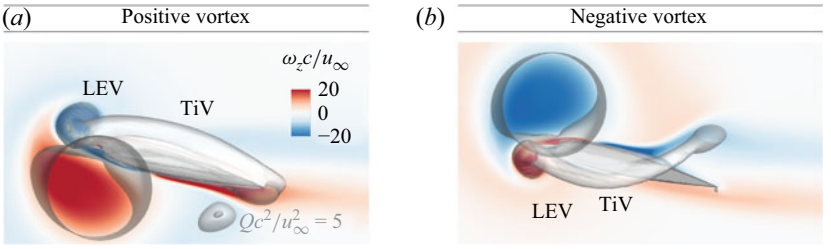


Figure 9. (*a*,*b*) Side view of the Q-criterion isosurface $Q = 5$ and colour contours of the spanwise vorticity ω_z along the root at $\tau = 0$ for the $(G, y_0/c) = (3, -0.25)$ and $(-3, 0.25)$ cases with the square wing.

because the development of the LEV was suppressed around $\tau = \tau_1$ due to the reversed TiVs. These attenuated positive-lift elements contribute to a mitigated positive-lift peak compared with the 2-D wing case.

Finally, to gain enhanced insights from the present results, we provide figure 9, where the side view of the Q-criterion and spanwise vorticity ω_z along the root at $\tau = 0$ are shown for $(G, y_0/c) = (3, -0.25)$ and $(-3, 0.25)$ with the square wing. For the case of the positive vortex encountering the square wing, as shown in figure 9(*a*), a strong compact LEV develops on the top surface, leading to a significant positive-lift peak. Furthermore, the TiVs strengthen through interaction with the gust vortex and generate large low-pressure cores above the wing, contributing to substantial vortex lift near the wingtips. However, the strengthened TiVs locally induce enhanced downwash and suppress further LEV development, attenuating the large lift peak compared to the 2-D wing. Notably, the large lift fluctuation is reduced when the square wing flies over the positive gust vortex as visualised in figure 9(*a*), due to smaller LEV development and a loss of negative-lift elements in the bottom-surface boundary layer by the impact.

Conversely, when the negative gust vortex encounters the square wing, as presented in figure 9(*b*), a strong compact LEV and reversed TiVs develop below the wing, resulting in a significant negative-lift peak. Simultaneously, the reversed TiVs locally induce upwash and suppress LEV growth, attenuating the lift peak compared with the 2-D wing. Opposite to the aforementioned positive gust vortex case, the large lift fluctuation caused by the negative gust vortex can be reduced by the wing flying under the gust vortex, as visualised in figure 9(*b*). These findings inform potential strategies for lift attenuation during extreme gust–finite-wing interactions by taking advantage of wing positions and TiVs.

4. Concluding remarks

This study identified key vortex dynamics that generates large lift fluctuations in extreme vortex-gust encounters by a square-planform wing and cause lift attenuation when compared with the case of a 2-D wing. We conducted direct numerical simulations of flows over an $sAR = 0.5$ wing at $Re = 600$ and performed lift element analysis on the unsteady flow field. We uncovered that TiVs play two opposing roles in the large lift changes during extreme vortex gust encounters by the finite wing: (i) contributing to the lift surge or drop by developing large low-pressure cores near the wingtips; (ii) mitigating the lift variations through three-dimensional vortex dynamics, such as enhanced downwash or upwash. The second effect dominates the first, causing the square wing to undergo a smaller lift change than the 2-D wing. In addition, we revealed effective vertical positions of the wing to reduce the lift change against an incoming gust vortex – flying over the positive gust vortex and flying beneath the negative one. The current insights obtained in the laminar flow setting can establish a foundation for extreme gust–finite-wing interacting flows and

https://doi.org/10.1017/jfm.2026.11728 Published online by Cambridge University Press

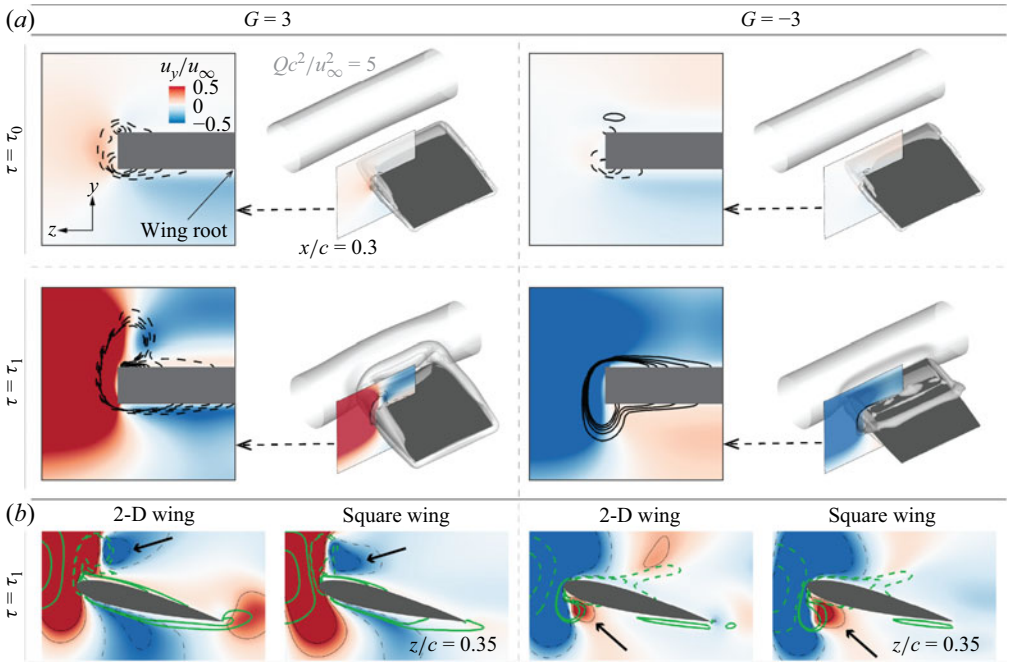


Figure 10. (*a*) Transverse velocity u_y (colour contours) and streamwise vorticity ω_x (line contours) along the streamwise slice $x/c = 0.3$ at $\tau = \tau_0$ and τ_1 for the cases of $G = 3$ and -3 with $y_0/c = 0$. Solid-line contours correspond to positive streamwise vorticity while dashed-line contours correspond to negative streamwise vorticity. (*b*) Velocity u_y (colour contours and black line contours) and ω_z (green line contours) around the 2-D wing and the spanwise slice along $z/c = 0.35$ of the square wing at $\tau = \tau_1$ for $G = 3$ and -3.

direct future efforts in developing control strategies or wing configurations to leverage TiV dynamics and mitigate large lift fluctuations at higher Reynolds numbers.

Funding. This work was supported by the US Department of Defense Vannevar Bush Faculty Fellowship (N00014-22-1-2798) and the Air Force Office of Scientific Research (FA9550-21-1-0174). H.O. acknowledges partial support from Honjo International Scholarship Foundation.

Declaration of interests. The authors report no conflict of interest.

Appendix A. Enhanced TiVs and reversed TiVs

We present in figure 10(*a*) the transverse velocity u_y and streamwise vorticity ω_x along the streamwise slice $x/c = 0.3$ at $\tau = \tau_0$ and τ_1 for the cases of $G = \pm 3$ with $y_0/c = 0$. For $G = 3$, the TiV grows in size and intensity from $\tau = \tau_0$ to τ_1. Regarding the $G = -3$ case, we can see coherent positive streamwise vorticity below the wing near the tip – the reversed TiV – at $\tau = \tau_1$, which is not present at $\tau = \tau_0$.

Additionally, in figure 10(*b*), we compare the transverse velocity u_y of the 2-D wing with the spanwise slice along $z/c = 0.35$ of the square wing for $G = \pm 3$. For $G = 3$, the region with a large downward velocity above the wing (indicated by the arrow in figure 10*b*) is located lower for the square-wing case compared with the 2-D wing case. This indicates the downwash effects of the enhanced TiVs. For $G = -3$, a larger upward velocity distribution below the wing is observed in the square-wing case compared with the 2-D wing case, suggesting the upwash effects of the reversed TiVs.

https://doi.org/10.1017/jfm.2026.11728 Published online by Cambridge University Press

	sAR	α	Re	Reference $\bar{C}_L$	Present $\bar{C}_L$
Zhang *et al.* (2020)	0.5	20°	400	0.32	0.31
Ribeiro *et al.* (2023)	2	14°	600	0.35	0.35

Table 1. Validation of the present simulation. Zhang *et al.* (2020) use an incompressible flow solver whereas the current study uses the compressible flow solver.

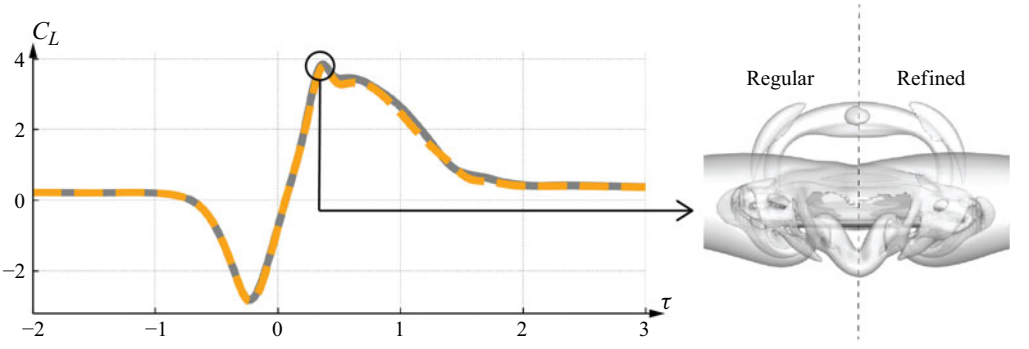


Figure 11. Lift coefficient change for the $(G, y_0/c) = (-3, 0)$ case with the regular and refined meshes. A front view of the instantaneous Q-criterion isosurface $Qc^2/u_\infty^2 = 6$ around the second lift peak is also shown for the two different meshes.

Appendix B. Verification and validation

We verify the grid convergence of the current mesh against a refined mesh. The current mesh, referred to as a regular mesh, consists of approximately 4.9×10^6 control volumes. The refined mesh comprised of approximately 2.4×10^7 control volumes includes increased resolution in all three spatial directions around the wing. Grid convergence is assessed by comparing the lift coefficient change and the instantaneous Q-criterion isosurface during the gust encounter with $(G, y_0/c) = (-3, 0)$, as shown in figure 11. We also validate the current mesh and numerical simulation with the time-averaged lift coefficient examined in Zhang *et al.* (2020) and Ribeiro *et al.* (2023), as shown in table 1. Based on these agreements, the regular mesh is deemed sufficient to perform the direct numerical simulations in this study.

References

Ahirwar, S., Swarnkar, R., Bhukya, S. & Namwade, G. 2019 Application of drone in agriculture. *Intl J. Curr. Microbiol. Appl. Sci.* **8** (01), 2500–2505.

Atassi, H.M. 1984 The Sears problem for a lifting airfoil revisited-new results. *J. Fluid Mech.* **141**, 109–122.

Barnes, C.J. & Visbal, M.R. 2018*a* Clockwise vortical-gust/airfoil interactions at a transitional Reynolds number. *AIAA J.* **56** (10), 3863–3874.

Barnes, C.J. & Visbal, M.R. 2018*b* Counterclockwise vortical-gust/airfoil interactions at a transitional Reynolds number. *AIAA J.* **56** (7), 2540–2552.

Brès, G.A., Ham, F.E., Nichols, J.W. & Lele, S.K. 2017 Unstructured large-eddy simulations of supersonic jets. *AIAA J.* **55**, 1164–1184.

Cai, G., Dias, J. & Seneviratne, L. 2014 A survey of small-scale unmanned aerial vehicles: recent advances and future development trends. *Unmanned Syst.* **2** (02), 175–199.

Chang, C.-C. 1992 Potential flow and forces for incompressible viscous flow. *Proc. R. Soc. Lond. A* **437** (1901), 517–525.

https://doi.org/10.1017/jfm.2026.11728 Published online by Cambridge University Press

CORDES, U., KAMPERS, G., MEISSNER, T., TROPEA, C., PEINKE, J. & HÖLLING, M. 2017 Note on the limitations of the Theodorsen and Sears functions. *J. Fluid Mech.* **811**, R1.
DALLMANN, U. 1988 Three-dimensional vortex structures and vorticity topology. *Fluid Dyn. Res.* **3** (1–4), 183.
DÉLERY, J.M. 2001 Robert Legendre and Henri Werlé: toward the elucidation of three-dimensional separation. *Annu. Rev. Fluid Mech.* **33** (1), 129–154.
FUKAMI, K., NAKAO, H. & TAIRA, K. 2024 Data-driven transient lift attenuation for extreme vortex gust-airfoil interactions. *J. Fluid Mech.* **992**, A17.
FUKAMI, K., SMITH, L. & TAIRA, K. 2025 Extreme vortex-gust airfoil interactions at Reynolds number 5000. *Phys. Rev. Fluids* **10** (8), 084703.
FUKAMI, K. & TAIRA, K. 2023 Grasping extreme aerodynamics on a low-dimensional manifold. *Nat. Commun.* **14**, 6480.
FULLER, J.R. 1995 Evolution of airplane gust loads design requirements. *J. Aircraft* **32** (2), 235–246.
GARMANN, D.J. & VISBAL, M.R. 2014 Dynamics of revolving wings for various aspect ratios. *J. Fluid Mech.* **748**, 932–956.
GOLDSTEIN, M.E. & ATASSI, H. 1976 A complete second-order theory for the unsteady flow about an airfoil due to a periodic gust. *J. Fluid Mech.* **74** (4), 741–765.
GUO, S., ESPINOSA DE LOS MONTEROS, J. & LIU, Y. 2015 Gust alleviation of a large aircraft with a passive twist wingtip. *Aerospace* **2** (2), 135–154.
HASSANALIAN, M. & ABDELKEFI, A. 2017 Classifications, applications, and design challenges of drones: a review. *Prog. Aerosp. Sci.* **91**, 99–131.
HE, S., GUO, S., LIU, Y. & LUO, W. 2021 Passive gust alleviation of a flying-wing aircraft by analysis and wind-tunnel test of a scaled model in dynamic similarity. *Aerosp. Sci. Technol.* **113**, 106689.
HERRMANN, B., BRUNTON, S.L., POHL, J.E. & SEMAAN, R. 2022 Gust mitigation through closed-loop control. II. Feedforward and feedback control. *Phys. Rev. Fluids* **7** (2), 024706.
HORLOCK, J.H. 1968 Fluctuating lift forces on aerofoils moving through transverse and chordwise gusts. *J. Basic Engng* **90** (4), 494–500.
HUNT, J.C.R., ABELL, C.J., PETERKA, J.A. & WOO, H. 1978 Kinematical studies of the flows around free or surface-mounted obstacles; applying topology to flow visualization. *J. Fluid Mech.* **86** (1), 179–200.
JONES, A.R. & CETINER, O. 2021 Overview of unsteady aerodynamic response of rigid wings in gust encounters. *AIAA J.* **59** (2), 731–736.
JONES, A.R., CETINER, O. & SMITH, M.J. 2022 Physics and modeling of large flow disturbances: discrete gust encounters for modern air vehicles. *Annu. Rev. Fluid Mech.* **54**, 469–493.
LEE, J.-J., HSIEH, C.-T., CHANG, C.C. & CHU, C.-C. 2012 Vorticity forces on an impulsively started finite plate. *J. Fluid Mech.* **694**, 464–492.
LOPEZ-DORIGA, B., JONES, A.R. & TAIRA, K. 2026 On the effect of airfoil geometry on extreme vortex-gust encounters. *J. Fluid Mech.* arXiv:2510.15154.
MA, R., YANG, Y., LI, M. & LI, Q. 2021 The unsteady lift of an oscillating airfoil encountering a sinusoidal streamwise gust. *J. Fluid Mech.* **908**, A22.
MARTÍNEZ-MURIEL, C. & FLORES, O. 2020 Analysis of vortical gust impact on airfoils at low Reynolds number. *J. Fluids Struct.* **99**, 103138.
MENON, K. & MITTAL, R. 2021 On the initiation and sustenance of flow-induced vibration of cylinders: insights from force partitioning. *J. Fluid Mech.* **907**, A37.
MISHRA, B., GARG, D., NARANG, P. & MISHRA, V. 2020 Drone-surveillance for search and rescue in natural disaster. *Comput. Commun.* **156**, 1–10.
MUELLER, T.J. & DELAURIER, J.D. 2003 Aerodynamics of small vehicles. *Annu. Rev. Fluid Mech.* **35** (1), 89–111.
ODAKA, H., LOPEZ-DORIGA, B. & TAIRA, K. 2026 Vortical similarities across laminar and turbulent extreme gust encounters. *J. Fluid Mech.* **1031**, R3.
PENG, D. & GREGORY, J.W. 2017 Asymmetric distributions in pressure/load fluctuation levels during blade-vortex interactions. *J. Fluids Struct.* **68**, 58–71.
PRESS, H. & MAZELSKY, B. 1954 A study of the application of power-spectral methods of generalized harmonic analysis to gust loads on airplanes. *Tech. Rep*. NACA-TR-1172.
RIBEIRO, J.H.M., NEAL, J., BURTSEV, A., AMITAY, M., THEOFILIS, V. & TAIRA, K. 2023 Laminar post-stall wakes of tapered swept wings. *J. Fluid Mech.* **976**, A6.
SMITH, L. & TAIRA, K. 2024 The effect of Reynolds number on the separated flow over a low-aspect-ratio wing. *J. Fluid Mech.* **992**, R2.
TAIRA, K. 2026 Extreme aerodynamics: a data-driven perspective. *Phys. Rev. Fluids* **11** (1), 014702.

https://doi.org/10.1017/jfm.2026.11728 Published online by Cambridge University Press

TAYLOR, G.I. 1918 On the dissipation of eddies. In *Meteorology, Oceanography and Turbulent Flow*, pp. 96–101. Cambridge University Press.

WANG, T., FENG, L.-H., CAO, Y.-T. & WANG, J.-J. 2024 Airfoil response to periodic vertical and longitudinal gusts. *J. Fluid Mech.* **979**, A35.

WU, Z., CAO, Y. & ISMAIL, M. 2019 Gust loads on aircraft. *Aeronaut. J.* **123** (1266), 1216–1274.

ZHANG, K., HAYOSTEK, S., AMITAY, M., BURTSEV, A., THEOFILIS, V. & TAIRA, K. 2020 Laminar separated flows over finite-aspect-ratio swept wings. *J. Fluid Mech.* **905**, R1.

https://doi.org/10.1017/jfm.2026.11728 Published online by Cambridge University Press